Influence of Laser Radar Sensor Parameters on Range Measurement and Shape Fitting Uncertainties

Christina Grönwall, Ove Steinvall, Fredrik Gustafsson, Tomas Chevalier

Division of Automatic Control
Department of Electrical Engineering
Linköpings universitet, SE-581 83 Linköping, Sweden
WWW: http://www.control.isy.liu.se
E-mail: stina@isy.liu.se, oveste@foi.se, fredrik@isy.liu.se, tomca@foi.se

16th October 2006

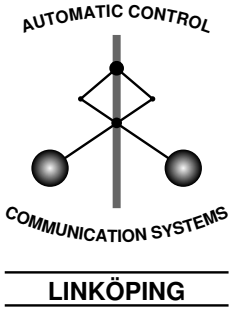

Report no.: LiTH-ISY-R-2745
Submitted to Optical Engineering

Technical reports from the Control & Communication group in Linköping are available at http://www.control.isy.liu.se/publications.

Abstract

In object reconstruction and recognition based on laser radar data, the range value's accuracy is important. The range data accuracy depends on the accuracy in the laser radar's detector, especially the algorithm used for time-of-flight estimation. In this paper, we model a general direct-detection laser radar system applicable for hard target measurements. We derive the time and range dependent laser radar cross sections for some simple geometric shapes (plane, cone, sphere, and parabola). The cross section models are used, in simulations, to find the proper statistical distribution of uncertainties in time-of-flight range estimations. Three time-of-flight estimation algorithms are analyzed; peak detection, constant fraction detection and matched filter. The detection performance for various shape conditions and signal-to-noise ratios are analyzed. Two simple shape reconstruction examples are shown, and the detector's performances are compared with the Cramér-Rao lower bound. The performance of the peak detection and the constant fraction detection is more dependent on the shape and noise level, compared to the matched filter. For line fitting the matched filter perform close to the Cramér-Rao lower bound.

Keywords: Range error, laser radar, time-of-flight, peak detection, matched filter, performance.

Contents

1 Introduction

In object reconstruction and recognition based on laser radar data, the range values are important. The accuracy in the reconstruction/recognition depends on the accuracy in range data. Further, the accuracy in the range data depends on the accuracy in the laser radar receiver, especially the algorithm used for time-of-flight estimation. The returning laser signal, used for time-of-flight estimations, will vary in shape depending on the object's shape, the atmosphere and the noise sources in the laser radar system.

In this paper, we model a general direct-detection laser radar system applicable for hard target measurements. We derive the time and range dependent laser radar cross sections for some simple geometric shapes (plane, cone, sphere and parabola). These shapes can describe the entire object or the part that is registered by an array element. The cross section models are used, in simulations, to find the proper statistical distribution for the range uncertainties and to analyze the impact of uncertainties in time-of-flight estimations. Three time-of-flight estimation algorithms are analyzed; peak detection, constant fraction detection, and matched filtering. The detection properties for various shape conditions and the detection properties as a function of the signal-to-noise ratio (SNR) are analyzed. These results apply when the beam diameter on the object is smaller than the object, which is typically the case for a laser range finder or a high-resolution scanning laser radar system. We also simulate a spatially resolved laser radar, similar to a generalized staring array. This gives the shape of the object which is used for shape fitting (shape reconstruction). Finally, we study the shape fitting properties, using range data computed with the different detectors.

The uncertainties in laser radar imaging performance and its effects on object recognition have been described by several authors [4, 9, 13]. In these papers the generated laser radar images are considered to be incoherent reflectance images that have properties similar to passive electro-optical (EO) imaging. The trade-off between range and spatial resolution is discussed in [12].

The uncertainties in laser radar ranging and the effects on object recognition are discussed in [6, 17, 18, 19]. In [18, 19] the accuracy and resolution of range data for a full waveform detector are analyzed. The most well-described uncertainties in range measurements depend on the optical signal-to-noise ratio, the atmospheric turbulence/scintillation effects and the uncertainty in beam pointing. In [17] the effects of the object's shape and reflection characteristics are analyzed. In [15], the range jitter due to the uncertainty for the laser emission time is estimated. Further, there are uncertainties in the estimates of time-of-flight in the received signal. Due to the interaction with the object, the atmosphere and the noise sources, the received signal will be broadened and noisy. This gives an uncertainty in determining the time-of-flight and hence an uncertainty in the range estimation.

In this paper we focus on a laser radar system that returns a single waveform. The main contributions are the description of the laser radar system in a channel model context [15], that the range uncertainty can be modelled as Gaussian distributed and the analysis of how the range uncertainty varies with shape and signal-to-noise ratio (SNR). The channel model of the laser radar systems clarifies the system's properties from a signal processing view. The results can be generalized to a system returning several echoes and waveform reconstruction

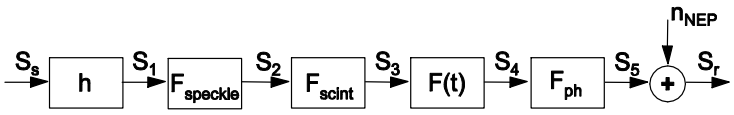

Figure 1: The laser beam propagation described using channel modelling.

but this is not the scope of this paper.

In Section 2, we present a sensor system model for a staring, monostatic, direct-detection system applicable for hard target measurements. The model includes object interaction, atmospheric effects, beam pointing error and receiver noise. Some common methods for time-of-flight estimation are listed in Section 3. In Section 4, the impulse responses for a few geometric shapes (flat surface, cone, sphere, and paraboloid) are derived. In Section 5, we validate the model and Sections 6 we apply the model to estimate the distribution of the ranging error. In Section 7 we use the model to discuss the impact of ranging error for shape fitting. The results are discussed in Section 8 and the paper is concluded in Section 9.

2 Sensor System Model

In this section we present the model of the laser radar system in a channel model context, see Figure 1. An ideal laser pulse, $S_s(x, y, t)$, is transmitted from the laser and a modified laser pulse, $S_r(x, y, t)$, is received in the receiver part of the system. The signal $S_r(x, y, t)$ is used for range estimation. The laser beam's interaction with the object and the atmosphere can be described as multiplicative (modulating) and additive factors that affect the sent laser pulse. The (sent) laser pulse's spatial and temporal shape is given by [19]:

$$S_s(x, y, t) = g(x, y) \left(\frac{t}{\tau}\right)^n \exp\left(-\frac{t}{\tau}\right), \tag{1}$$

where $g(x, y)$ is the beam's spatial shape (usually modeled as Gaussian). The parameter n indicates the laser pulse's temporal shape. For a normal Q-switched pulse $n = 1$ usually gives a good fit. The full width half maximum (FWHM) for $n = 1$ is given by $T_p = 3.5\tau$. For $n = 2$ a more sharp and symmetric pulse is obtained and we have $T_p = 1.22\tau$. Normally, T_p is 1-5 ns.

For a measurements on a hard target with a monostatic system, the laser beam interacts with the object according to

$$S_1(x, y, t) = h(x, y, t) S_s(x, y, t), \tag{2}$$

where $h(\cdot)$ is the object's impulse response, based on the object's geometrical and reflectance properties. Some examples of object impulse responses are given in Section 4. The impulse response, i.e., the object cross section, is given by

$$h(x, y, t) = 4\pi\rho_b(x, y)\delta(t - 2z(x, y)/c),$$

where $\delta(\cdot)$ is the Dirac function. The object reflection ρ_b is modeled by the bidirectional reflection distribution function (BRDF) [17]

$$\rho_b(x, y, \theta) = \frac{A}{\cos^6 \theta} \exp\left(-\frac{\tan^2 \theta}{s^2}\right) + B \cos^m \theta,$$

where the first part describes the specular components and the second part the diffuse components for the incidence angle θ. Beam jitter, due to pointing error, can be modeled by translation of $g(x, y)$ relative to $h(x, y, t)$. If we add speckles, F_{speckle} and turbulence-induced scintillations, F_{scint}, we have

$$S_3(x, y, t) = (h(x, y, t) * S_s(x, y, t)) F_{\text{speckle}} F_{\text{scint}}. \tag{3}$$

The turbulence-induced scintillations can be modeled as a Log-normal distributed multiplication factor [1]:

$$F_{\text{scint}} \in 1/S_{\text{av}} \mathcal{LN}\left(-\frac{1}{2}\sigma^2_{\ln \text{I}}, \sigma_{\ln \text{I}}\right),$$

where S_{av} is the time average of the signal S and $\sigma_{\ln \text{I}}$ is the aperture-averaged and time-compensated log-intensity variance. The speckle properties is modeled by a Gamma distributed multiplication factor [5]

$$\begin{aligned} F_{\text{speckle}} &\in \Gamma(M, S_{\text{av}}/M) \\ M &= D_{\text{rec}}/D_{\text{speckle}}, \end{aligned}$$

where D_{rec} is the receiver's aperture diameter and D_{speckle} is the average diameter of a speckle cell at the receiver.

Various laser and receiver properties are described by the received peak power factor [10]

$$F(t) = \frac{E_p}{2\tau} \exp(-2\sigma_{\text{atm}} R) \frac{r^2_{\text{aper}}}{R^2} T_r,$$

where E_p is the total pulse energy, σ_{atm} is the atmosphere's damping, R is the (slant) range to the object, r_{aper} is the receiver's aperture and T_r is the receiver's total transmission. Including these effects we have

$$S_4(x, y, t) = S_3(x, y, t) F(t) \tag{4}$$

The noise sources in the laser radar system consist of system jitter, noise equivalent power (NEP). The system jitter variance σ^2_{sj}, that gives beam pointing error, can for a small jitter be included in the log-intensity variance as

$$\sigma^2_{\ln \text{I,tot}} = \sigma^2_{\text{sj}} + \sigma^2_{\ln \text{I}}$$

and included in the scintillation process. The main noise contributions in the NEP come from the detector and the amplifier. The standard deviation of the NEP is modeled

$$\sigma^2_{\text{NEP}} = \sigma^2_{\text{NEP,detector}} + \sigma^2_{\text{NEP,amplifier}}.$$

The NEP uncertainty in the received signal, is approximated by a Gaussian distribution, i.e.,

$$n_{\text{NEP}}(t) \in \mathcal{N}\left(0, \sigma^2_{\text{NEP}}\right).$$

A measurement depends on that photons are reaching the receiver's detector. The photons' arrival at the detector is modeled by a Poisson process

$$F_{\text{ph}} \in \text{Po}\left(m\right),$$

where m is the mean number of arrivals within a time interval T [16]. In hard target measurements good conditions are usually assumed, which means that many photons are detected in every time interval. In this case the detection probability at the detector is close to 1, thus $F_{\text{ph}} = 1$.

Including these noise sources we end up with a received signal as

$$\begin{aligned} S_r\left(x,y,t\right) &= S_4\left(x,y,t\right) + n_{\text{NEP}}\left(t\right) && \text{(5a)} \\ &= S_s\left(x,y,t\right) h(x,y,t) F_{\text{speckle}} F_{\text{scint}} F\left(t\right) + n_{\text{NEP}}\left(t\right). && \text{(5b)} \end{aligned}$$

The signal S_r can be divided into one part that is a function of both time and space and one part that is only time dependent:

$$\begin{aligned} S_r\left(x,y,t\right) &= S_{r1}\left(x,y,t\right) S_{r2}\left(t\right) + n_{\text{NEP}}\left(t\right), \\ S_{r1}\left(x,y,t\right) &= 4\pi g(x,y)\rho_b(x,y)\delta(t - 2z\left(x,y\right)/c), \\ S_{r2}\left(t\right) &= \left(\frac{t}{\tau}\right)^n \exp\left(-\frac{t}{\tau}\right) F_{\text{speckle}} F_{\text{scint}} F\left(t\right). \end{aligned}$$

This signal is used for estimation of time-of-flight, from which the object range is calculated, see Section 3. The estimated object range can be considered a function of $S_r\left(x,y,t\right)$,

$$\hat{R}\left(x,y,z\right) = f_1\left(S_r\left(x,y,t\right)\right). \tag{6}$$

This relation is analyzed in Section 6. Range data can later be used for shape fitting, where the parameter vector θ described the estimated shape:

$$\hat{\theta} = f_2\left(\hat{R}\left(x,y,z\right)\right), \tag{7}$$

which is analyzed in Section 7.

3 Detection Methods

There are three common detection schemes; peak detection, constant fraction discrimination (also called 50% leading edge detection), and matched filter detection (also called correlation detection). For peak detection the estimated object range $\hat{R}$ is calculated using the time-of-flight corresponding to the largest value in $S_r\left(t\right)$, i.e.,

$$\hat{R}_{\text{PD}} = f_{\text{PD}}\left(S_r\left(t\right)\right) = \frac{c}{2} \arg\max_t S_r\left(t\right) - \hat{R}_{\text{PD}}^{\text{offset}}. \tag{8}$$

For constant fraction the rising edge at half peak power is detected, i.e.,

$$\hat{R}_{\text{CF}} = f_{\text{CF}}\left(S_r\left(t\right)\right) = \frac{c}{2} \text{sol}_t \left\{ S_r\left(t\right) = \frac{1}{2} \max_t S_r\left(t\right) \right\} - \hat{R}_{\text{CF}}^{\text{offset}}. \tag{9}$$

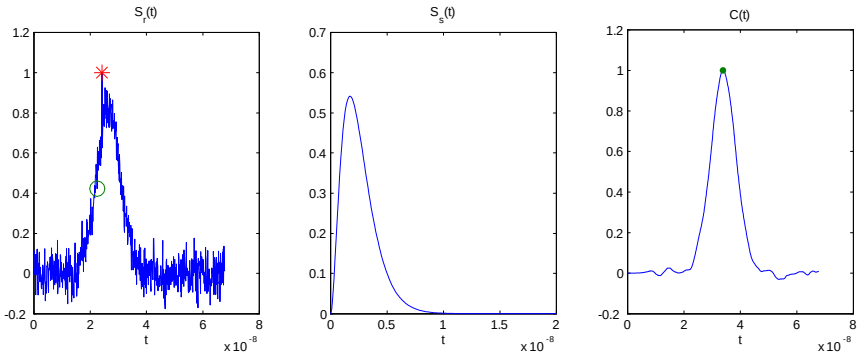

Figure 2: Example of detections. Left: the returning pulse $S_r(t)$ with peak detection (*) and constant fraction (o). Middle: $S_s(t)$, Right: matched filter output $C(t)$ with peak detection (*). Arbitrary axis.

and for the matched filter we correlate the output signal with the input signal. The correlation peak gives the estimated time-of-flight

$$\begin{aligned} C(t) &= S_r(t) * S_s(-t), \\ \hat{R}_{\mathrm{MF}} &= f_{\mathrm{MF}}(S_r(t)) = \frac{c}{2} \arg\max_t C(t) - \hat{R}_{\mathrm{MF}}^{\mathrm{offset}}, \end{aligned} \tag{10}$$

where $*$ is convolution in time. A detection example is shown in Figure 2.

In all detection methods we compensate for the rise time in $S_s(t)$, the offsets are determined by applying the algorithms on the input signal:

$$\begin{aligned} \hat{R}_{\mathrm{PD}}^{\mathrm{offset}} &= \frac{c}{2} \arg\max_t S_s(t) \\ \hat{R}_{\mathrm{CF}}^{\mathrm{offset}} &= \frac{c}{2} \mathrm{sol}_t \left\{ S_s(t) = \frac{1}{2} \max_t S_s(t) \right\} \\ \hat{R}_{\mathrm{MF}}^{\mathrm{offset}} &= \frac{c}{2} \arg\max_t S_s(t) * S_s(-t) \end{aligned}$$

4 Impulse Response for Some Common Geometric shapes

In [17], the time independent cross sections, or impulse responses, for planes, spheres, paraboloids and cones are given. Below we will derive the time and spatially dependent impulse responses for a plane, cone, sphere and paraboloid. For details we refer to [7]. We assume that the laser beam is centered around the object's rotational symmetry axis.

4.1 Time and Range Dependent Impulse Responses

The impulse response for the time and spatially dependent cross section is given by

$$h(x, y, t) = 4\pi g(x, y) \rho_b(x, y) \delta(t - 2R(x, y)/c).$$

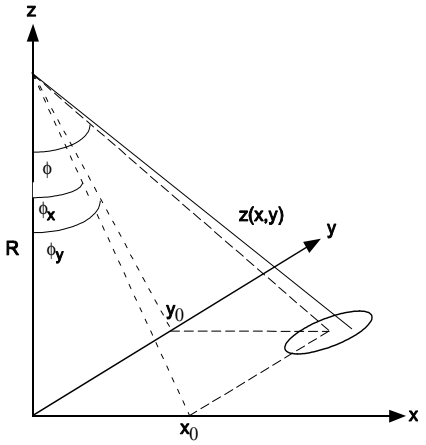

Figure 3: Geometry for plane surface.

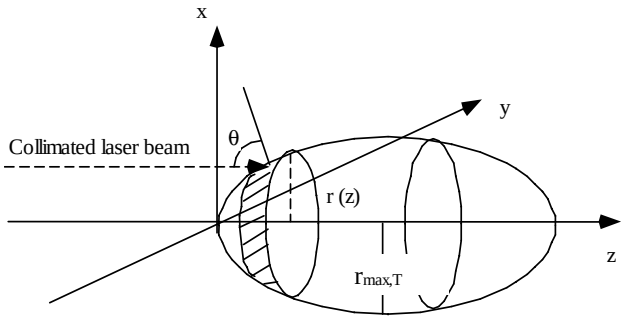

Figure 4: Geometry for rotation-symmetric objects.

The laser beam's spatial shape is included as it effects the cross section. For all cases we assume that the BRDF function is constant over the object surface and only depends on the incident angle θ, i.e., $\rho_b(x,y) = \rho_b(\theta)$ and that the beam profile is Gaussian, i.e.

$$g(x,y) = \exp\left(-\frac{(x-x_0)^2 + (y-y_0)^2}{\left(w/\sqrt{2}\right)^2}\right),$$

where w if the laser beam's radius. In Figure 3 we define the geometry for a measurement on a **plane** with angle of incidence equal to ϕ. If the laser beam is elliptic with approximately no spread in y, we have $R(x,y) \approx x/\sin\phi_x$. For the 2D case, we have $R(x,y) \approx x/\tan\phi_x\sqrt{1+\tan^2\phi_x+\tan^2\phi_y}$ and the impulse response is [7]

$$h_{\text{plane}}(x,y,t) = \exp\left(-2\frac{(x-x_0)^2 + (y-y_0)^2}{w^2}\right)\delta\left(t - \frac{2R(x,y)}{c}\right). \quad (11)$$

If we assume that the laser beam axis and the z axis coincide, i.e., $\phi = 0$, and that we have rotation-symmetric objects we can use polar coordinates (r,ω), see Figure 4. The impulse response can now be written

$$h(r,\omega,t) = 4\pi\exp\left(-\frac{r^2}{\left(w/\sqrt{2}\right)^2}\right)\rho_b(\theta)\delta\left(t - 2z(r,\omega)/c\right), \quad (12)$$
$$0 \le r \le w = r_{\text{beam}}, \quad 0 \le \omega \le 2\pi.$$

- For a **cone** with half-angle α, where $\alpha = \pi/2 - \theta$, we have $z(r,\alpha) = r/\tan\alpha$ or, equivalently, $z(r,\theta) = r/\tan(\pi/2-\theta)$. The BRDF function can be modeled as $\rho_b(\pi/2-\alpha)$. By setting $\alpha = \pi/2$ we get the laser radar cross section for a **flat plane**.
- For a **sphere** we have $\omega = \theta$ and $z(r) = r_T - \sqrt{r_T^2 - r^2}$, where r_T is the sphere's radius. If we assume that the sphere's surface is Lambertian [10], we have $\rho_b(\theta) = \cos\theta = \sqrt{1 - r^2/r_T^2}$.
- For an elliptic **paraboloid** with coefficient k we have $z(r) = kr^2$. For a Lambertian surface, we have $\rho_b(\theta) = \cos\theta = 1/\sqrt{1+(rk)^2}$.

Inserting these expressions in (12) we get

$$h_{\text{cone}}(r,t) = 4\pi\rho_b(\pi/2-\alpha)\exp\left(-2\frac{r^2}{w^2}\right)\delta\left(t - \frac{2r}{c\tan\alpha}\right), \quad (13)$$

$$h_{\text{sphere}}(r,t) = 4\pi\sqrt{1-r^2/r_T^2}\exp\left(-2\frac{r^2}{w^2}\right)\delta\left(t - \frac{2r_T}{c}\left(1 - \sqrt{1-r^2/r_T^2}\right)\right), \quad (14)$$

$$h_{\text{paraboloid}}(r,t) = 4\pi\frac{1}{\sqrt{1+(rk)^2}}\exp\left(-2\frac{r^2}{w^2}\right)\delta\left(t - \frac{2kr^2}{c}\right). \quad (15)$$

4.2 Time Dependent Impulse Responses

The time-only dependent expressions are retrieved by integrating over the surface (x, y, z) or radius r, respectively, and using the properties of the Dirac function [7]. For the plane, we have

$$h_{\text{plane}}(t) = \sqrt{\frac{\pi}{2}} \frac{cw}{k} \exp\left(-\left(\frac{t-t'}{\tau_0}\right)^2\right), \tag{16a}$$

$$k = 1/\tan\phi_x \sqrt{1 + \tan^2\phi_x + \tan^2\phi_y}, \tag{16b}$$

$$t' = 2kx_0/c, \tag{16c}$$

$$\tau_0 = \sqrt{2}kw/c, \tag{16d}$$

and for the rotation-symmetric objects we have

$$h_{\text{cone}}(t) = 2\pi\rho_b(\pi/2 - \alpha)c\tan\alpha \exp\left(-\frac{(ct\tan\alpha)^2}{2w^2}\right), \tag{17}$$

$$h_{\text{sphere}}(t) = \frac{\pi}{2r_T}\sqrt{\frac{c}{t}}\frac{(2r_T - ct)^2}{\sqrt{4r_T - ct}} \exp\left(-\frac{ct(4r_T - ct)}{2w^2}\right), \tag{18}$$

$$h_{\text{paraboloid}}(t) = \pi \frac{1}{\sqrt{\frac{kt}{2c} + \left(\frac{kt}{2}\right)^2}} \exp\left(-\frac{ct}{kw^2}\right). \tag{19}$$

5 System Model Validation

The system model (5) is validated with real waveform data from a scanning system[1]. We do not have enough information about the real laser radar system and the simulated waveform is found using gray-box identification. The validation data consists of three measurements on a gravel road, with measurement set-up according to Table 1. Using this data we can validate the impulse response expression for the plane model. The real waveforms and the simulation result are shown in Figure 5. The simulated signal follows the real signals except for the last down-going flank. This is probably due to (for the authors) unknown time constants in the receiver electronics. Unevenness in the road may also affect the returning waveform. The noise in the simulated system is similar to the noise in real data. We believe that the model describe the system dynamics in large and is valid for our analysis.

6 Impact of Uncertainties in the Time-of-Flight Estimation

We will now use the model to analyze the properties of the detection methods (8)-(10). In other words, the expression (6) is studied. For the time dependent impulse response, we will study the detection properties for various shape conditions and the detection properties as a function of the signal-to-noise ratio

[1] Data comes from the TopEye system, see www.topeye.com.

Table 1: Parameter values used in the validation.

Laser radar	**Value**	**Object**	**Value**
Wavelength (λ)	1.064 μm	BRDF (A, s, B, m)	$\left(0, 10^{-6}, 0.5, 1\right)$
Beam divergence	10^{-3} rad	Vertical range $z = R\,(0, 0)$	215 m
Beam shape n	1.9	Object slant angle ϕ	20 deg
Beam shape τ	$T_p/1.4$		
T_p	4 ns	**Atmosphere**	**Value**
E_p	$3 \cdot 10^{-6}$ J	D_{speckle}	0.0011 m
r_{aper}	0.05 m	$\sigma_{\ln \text{I}}$	$4.94 \cdot 10^{-5}$
T_r	0.7	σ_{atm}	$5.53 \cdot 10^{-6}$ m^{-1}
S_{av}	1		
D_{rec}	0.1 m	**Simulation**	**Value**
$\sigma_{\text{NEP,detector}}$	$9.91 \cdot 10^{-8}$ W	Time resolution	10^{-9} s
$\sigma_{\text{NEP,amplifier}}$	$8.0 \cdot 10^{-8}$ W	Range resolution	*n.a.*
σ_{sj}	0		

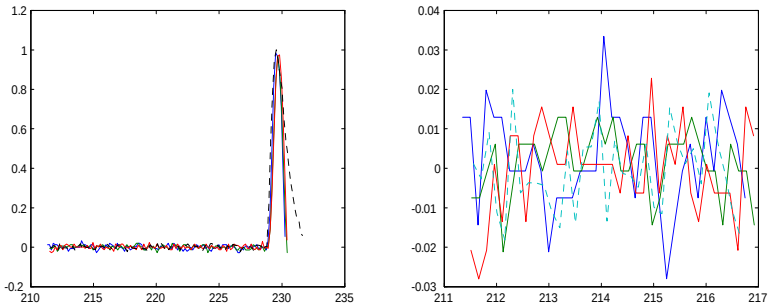

Figure 5: Model validation. Solid lines: measurements from the real laser radar system, dashed: simulation. Left: whole waveform, right: noise part.

Table 2: Parameter values used in the simulations.

Laser radar	**Value**	**Object**	**Value**
Wavelength (λ)	1.06 μm	BRDF (A, s, B, m)	$\left(0, 10^{-6}, 1, 1\right)$
Beam divergence	10^{-3} rad	Vertical range $z = R\,(0, 0)$	1000 m
T_p	3 ns		
Beam shape n	1	**Atmosphere**	**Value**
Beam shape τ	$T_p/3.5$	D_{speckle}	0.0011 m
E_p	10^{-3} J (SNR fix)	$\sigma_{\ln \text{I}}$	$1.2 \cdot 10^{-4}$
E_p	$10^{-6} - 10^{-2}$ J (SNR vary)	σ_{atm}	$5.5 \cdot 10^{-5}$ m^{-1}
r_{aper}	0.05 m		
T_r	0.7	**Simulation**	**Value**
S_{av}	1	Time resolution	10^{-10} s
D_{rec}	0.1 m	Range resolution	0.01 m
$\sigma_{\text{NEP,detector}}$	$9.9 \cdot 10^{-8}$ W		
$\sigma_{\text{NEP,amplifier}}$	$8.0 \cdot 10^{-8}$ W		
σ_{sj}	0		

(SNR). The detection properties are studied by the estimation error in the range estimate

$$\Delta R = \hat{R} - R_0,$$

where $\hat{R}$ is estimated with one of the detection algorithms and R_0 is the true range. We define SNR as

$$SNR = \frac{\max |S_r|}{\sigma_{\text{NEP}}}.$$

The parameter settings that are used in the simulations are summarized in Table 2. The simulations are performed in Matlab[2]. We assume that the atmosphere's impact is low (low turbulence and long visual range) and that there is no beam jitter present. The object's surface have Lambertian properties. The beam divergence is 10^{-3} rad, which results in a beam radius of approximately 0.5 m on the object.

6.1 Determination of Range Error Distribution

The distribution of the range errors has been determined by fitting several data sets to some common statistical distributions, among them exponential and Gaussian distribution. The Gaussian distribution is estimated by the algorithm `normfit.m`, which returns 95% confidence intervals for the parameter estimates. In Figure 6 a range error histogram and the estimated Gaussian distribution are shown. Similar results were obtained for all simulations in this paper.

For this simulation of measurements on a plane with $\phi_x = 5\,\text{deg}$, we can see that the peak detection and matched filter are unbiased while the leading edge

[2]Matlab is a product of The Mathworks, Inc., see www.mathworks.com.

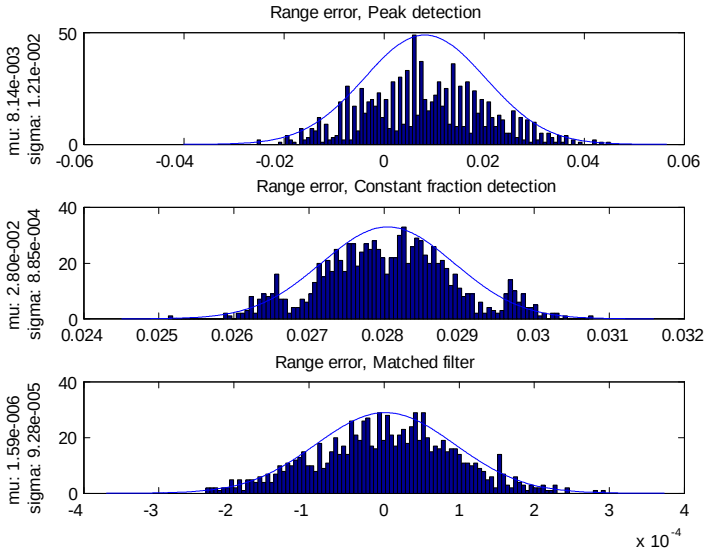

Figure 6: Histogram of 1000 simulations and estimated Gaussian distribution for a plane with $\phi_x = 5\,\text{deg}$. The estimated means and standard deviations are given to the left of the curves. Top: peak detection, middle: constant fraction detection, bottom: matched filter. Values given in meters.

detector contains bias. The standard deviation is approximately 10^{-2} meter for the peak detection. The standard deviation in the constant fraction detection is ten times smaller and for the matched filter hundred times smaller, compared to the peak detection. We draw the conclusion that in this type of system the range error can be modeled as Gaussian distributed.

6.2 Range Error Properties for Various Shapes

In this test we vary the object's shape properties while having SNR constant and large (SNR$= 7 \cdot 10^3 \approx 38$ dB). For the plane (16), the tilt angle ϕ_x ($\phi_y = 0$) will vary, for the cone (17) we vary the half-cone angle and for the paraboloid (19) we vary the coefficient k. For the sphere (18) we vary the relation between the beam radius r and the object radius r_T, defined as

$$k_T = r_T/r.$$

For the cone and parabola we set $k_T = 10$. For each object setup, we estimate the range 1000 times and estimate the Gaussian distribution for the data set.

The results for the different object types are shown in Figures 7-10, the estimated mean value $E(\Delta R)$ and standard deviation std(ΔR) are shown. For all shapes, the peak detection has a very large standard deviation compared to constant fraction detection and matched filter detection. The results for the plane indicates that constant fraction detection is not satisfactory when the plane deviates from being perpendicular to the laser beam. For all detection methods, the error increases when the pulse is broadened, i.e., when ϕ_x increases.

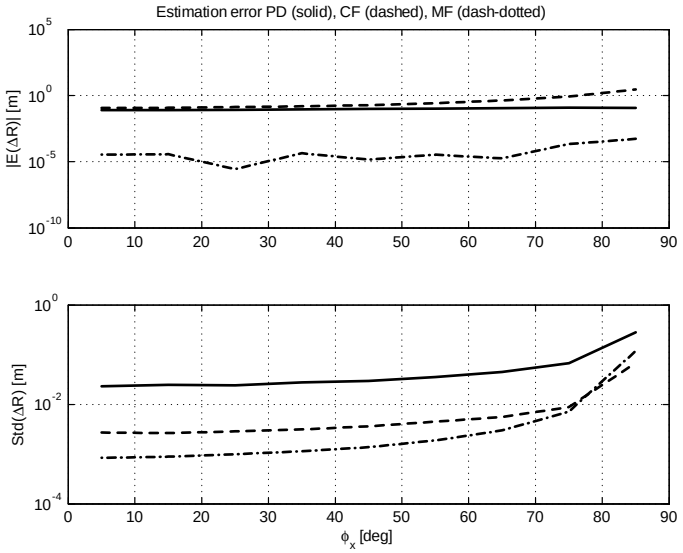

Figure 7: The $|E(\Delta R)|$ and std(ΔR) as a function of slant angle ϕ_x for a plane.

For the cone can we see that the estimation error decreases when the half-cone angle increases. This is expected, as the cone approaches a vertical flat plane when the half-cone angle increases. The range estimation error is very small for both spheres and parabolas. For the sphere the surface that the laser beam hits have decreasing curvature when k_T increases, this explains the decreasing estimation error. In this case the matched filter has the best performance. For the parabola, the curvature increases when k increases, which explains the small variation in the estimation error for different k values. Also in this case the matched filter has the best performance. After these tests we conclude the range error can be modeled as Gaussian distributed, with bias b and variance σ_R^2 that varies with the object's shape, i.e.,

$$\Delta R \in \mathcal{N}\left(b, \sigma_R^2\right).$$

6.3 Range Error as a Function of SNR

In this case we calculate the statistics of the range error as a function of SNR. The SNR is varied by varying the laser peak power E_p. The tests are performed for a plane (16) with $\phi_x = 5\,\text{deg}$ and a sphere (18) with $k_T = 10$. The Gaussian distribution is estimated using the same approach as above.

The results are shown in Figures 11-12. For all cases, the mean and standard deviation of the estimation error decrease when the SNR increases. The matched filter is less affected by the noise compared to the other detection methods. Both the peak detection and the constant fraction detection produces rather high bias. The peak detection method has a rather large standard deviation even when the SNR is high.

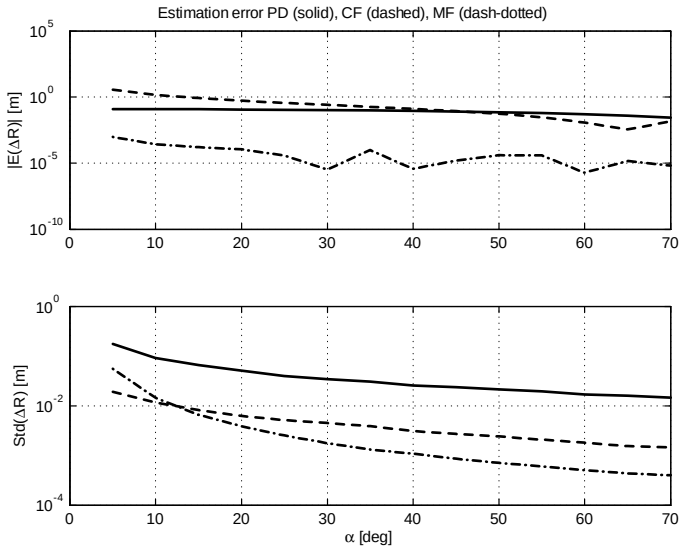

Figure 8: The $|E(\Delta R)|$ and std(ΔR) as a function of half-cone angle α for a cone.

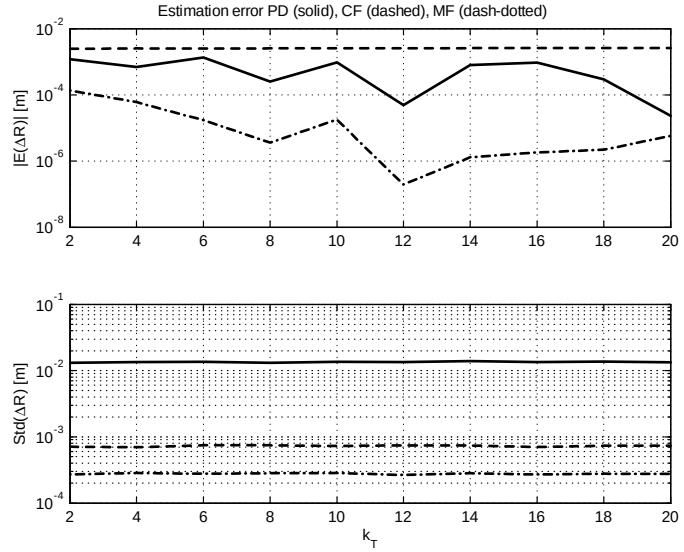

Figure 9: The $|E(\Delta R)|$ and std(ΔR) as a function of k_T for a sphere.

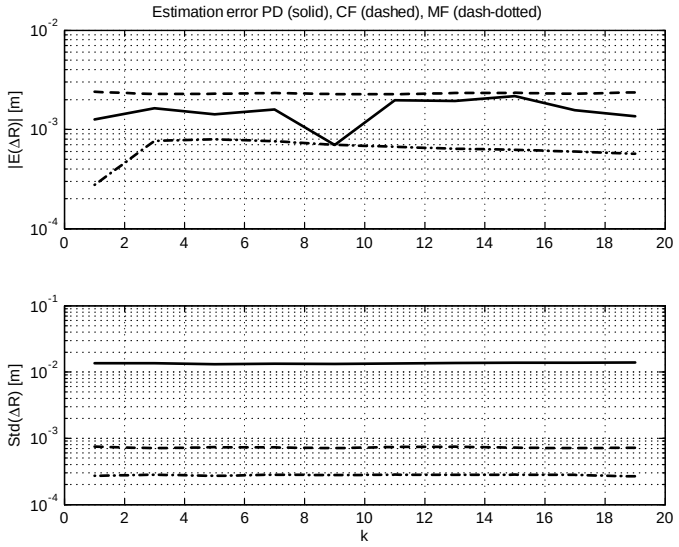

Figure 10: The $|E(\Delta R)|$ and std(ΔR) as a function of parabola curve coefficient k.

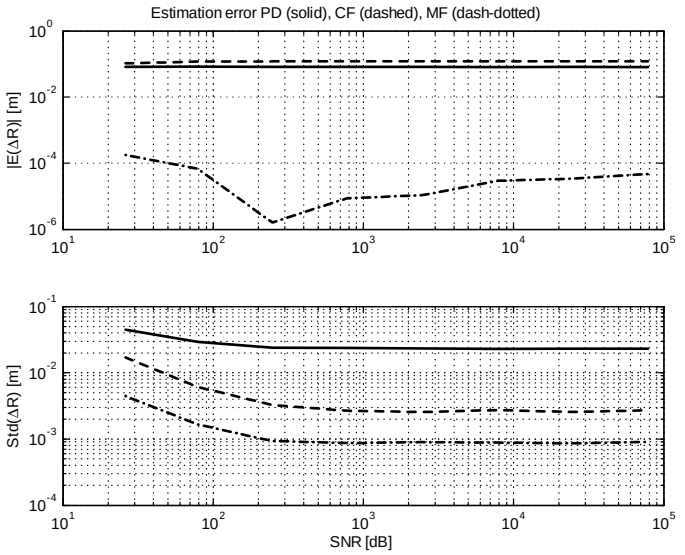

Figure 11: The $|E(\Delta R)|$ and std(ΔR) as a function of SNR for a plane with $\phi_x = 5\,\mathrm{deg}$.

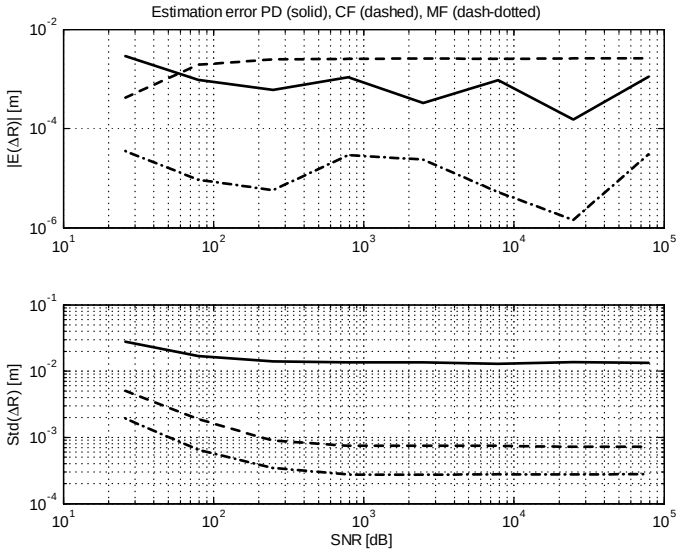

Figure 12: The $|E(\Delta R)|$ and std(ΔR) as a function of SNR for a sphere with $k_T = 10$.

7 Impact of Range Error in Shape Fitting

A common step in object reconstruction and recognition is surface/shape fitting. In this section we study the expression (7) further. Based on the previous section we can model range data as

$$\hat{R}(x, y, z) \in \mathcal{N}\left(R^0 + b, \sigma_R^2\right),$$

where R^0 is the true but unknown range, b and σ_R^2 are the shape and SNR dependent bias and variance, respectively. The estimation variance in the shape's parameter can be expressed as a function of the true parameter values and the total uncertainty in the system, using the Cramér-Rao lower bound (CRLB) [11]. The CRLB describes the lower bound for the variance error of an unbiased estimator. The lower limit can be reached if the estimator is defined as minimum variance and unbiased [11]. For parameter θ the CRLB is written

$$\text{CRLB} \leq \text{Var}\left(\hat{\theta}\right).$$

An approach for model-based plane fitting, based on measurement error regression, is described in [3]. A plane in (x, y, z) is described as

$$n_1 x + n_2 y + n_3 z + c = 0 \tag{20a}$$
$$n_1^2 + n_2^2 + n_3^2 = 1, \tag{20b}$$

where the normal vector $\mathbf{n} = (n_1, n_2, n_3)^T$ defines the tilt of the plane and c the distance to origin. The parameters in the model are $\theta_{\text{plane}} = (n_1, n_2, n_3, c)$. The CRLB expression for a line/plane parameter estimation in noise can be found in [6]. The sphere is modeled as

$$x = z_1' + r' \cos\omega \sin\gamma \tag{21a}$$
$$y = z_2' + r' \sin\omega \sin\gamma, \tag{21b}$$
$$z = z_3' + r' \cos\gamma, \tag{21c}$$

where the (z_1', z_2', z_3') is the origin and r' is the radius of the sphere. The parameter vector is $\theta_{\text{sphere}} = (z_1', z_2', z_3', r')$.

We will present shape fitting of lines and circles and investigate how the parameter estimation performance depends on the detection principle. The shape fitting properties, using data detected with the different detectors, is studied in increasing noise. Parametric fit of line and circle are used and the detectors' performances are evaluated in terms of correctness in parameter estimate. There are 100 samples equally distributed over the surface. The statistical properties of the estimates are studied by the mean squared error (MSE) and bias, which are averaged over 100 sets. The MSE and the bias for parameter θ_j are defined as

$$\begin{aligned} \text{MSE}\left(\hat{\theta}_j\right) &= E\left(\hat{\theta}_j - \theta_j^0\right)^2 + E^2\left(\hat{\theta}_j - \theta_j^0\right) \\ &= \text{Var}\left(\hat{\theta}_j\right) + \text{bias}^2\left(\hat{\theta}_j\right), \end{aligned}$$

where θ_j^0 is the true, but unknown, parameter and $\hat{\theta}_j$ is the estimate.

We use the time and range dependent impulse response in Section 4.1. For the plane model (11) we set $\phi_x = 5\,\text{deg}$ and $\phi_y = 0$ to get a line. The parametric line description used in line fitting is achieved by setting $n_3 = 0$ in (20). The line is fitted using the mixed least squares-total least squares algorithm [3, 8], which allows errors in variables. The circle model equals the sphere model (14) and we set $k_T = r_T/r = 1$. In the parametric sphere description used for circle fitting (21) we set $\gamma = \pi/2$ and $z_3' = 0$. The circle fitting algorithm [2] is iterative and needs initialization. We initialize with the true parameters, which means that we get the best possible performance of the algorithm.

Examples of range data detected with the matched filter and estimated curves are shown in Figure 13. The statistics for the fitting results are shown in Figures 14-15. The input (range) data is not compensated for bias, which means that the bias is transferred to the parameter estimation. The parameter estimations produced using peak detection and constant fraction contain bias and have quite large standard deviation, especially for line fitting. For both the line and the circle the matched filter is less affected by the noise compared to the other detection methods.

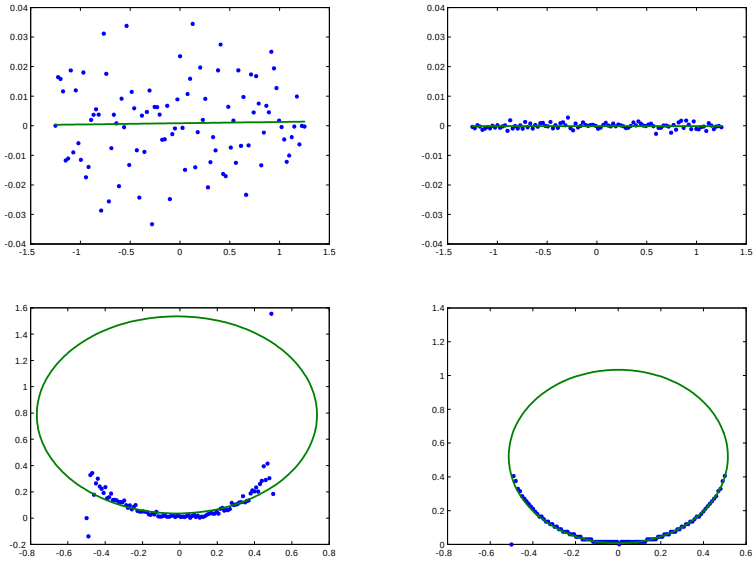

Figure 13: Example of shape fitting based on matched filter detection. Top: line fitting with low SNR (left) and high SNR (right). Bottom: circle fitting with low SNR (left) and high SNR (right).

When there is additive Gaussian white noise, the matched filter is a realization of the optimal detector [14]. This implies that the range error can be applied as input uncertainty in the CRLB calculation. Usually a theoretical value of σ_R is used. This is not available in this case and the variance estimated by the matched filter is used instead. The CRLB limit is shown in Figure 14, the limit is close to the matched filter result. This is expected for an efficient estimator as the matched filter, that produces range estimates with very small bias.

8 Discussion

In this paper we model a laser radar system that is not subject to beam jitter. For the single pulse simulations, Section 6, the results are applicable to both scanning and staring systems. For the simulation of a sensor array, Section 7, the results are applicable for an idealized staring sensor. To simulate a scanning array, the beam jitter must be included. The beam jitter can be modeled by multiplying the laser pulse (1) with a Gaussian distributed point direction (x, y).

We also assume that we have good measurement conditions where the number of signal photo electrons exceed the noise electrons. In the case of few returning photons, the Poisson process will have larger impact on the returning pulse. This is discussed in [16].

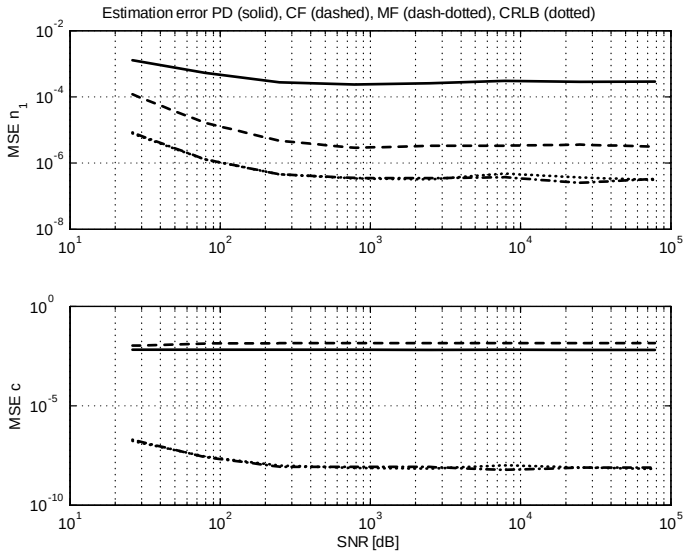

Figure 14: The MSE of parameter estimates as a function of SNR for line with $\phi_x = 5\,\mathrm{deg}, \phi_y = 0\,\mathrm{deg}$.

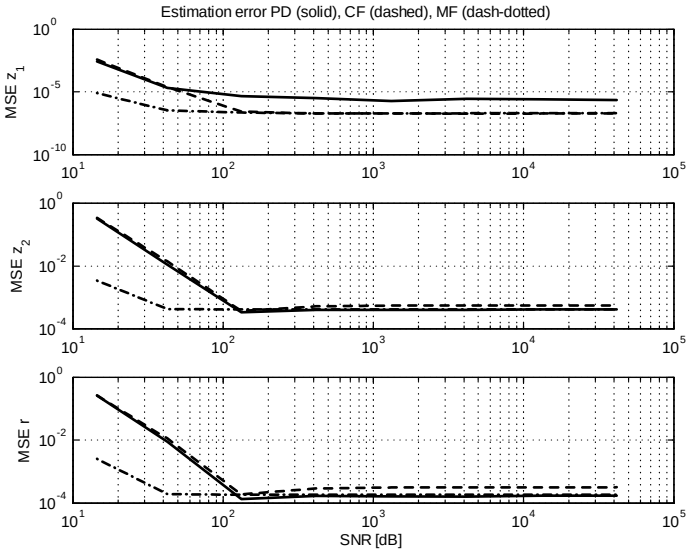

Figure 15: The MSE of parameter estimates as a function of SNR for circle with $k_T = 1$.

In all tests performed in this paper the matched filter has the best performance. For all shapes, the peak detection has a very large standard deviation compared to constant fraction detection and matched filter detection. The performance of the peak detection and the constant fraction detection is more dependent on the shape, compared to the matched filter. Further, the matched filter is less affected by the noise compared to the other detection methods. The properties of the matched filter, see for example [14], gives that it is an optimal detector in additive white Gaussian noise, which is the case in these tests. Further, the output SNR from a matched filter depends on the energy of the returned signal rather than its detailed characteristics. This results in an output signal with few fluctuation from the matched filter, which simplifies the following peak detection.

If we compare scanning and staring laser radar systems, the type of uncertainties and their impact differ. For example, the spatial uncertainty between the samples will be larger in a scanning system due to beam jitter. It would be interesting to compare the range accuracy and resolution for a scanning system with that of a staring system. The performance of both system types can be modeled using the ideas presented in this paper.

The results show that the matched filter detection usually has better performance compared to peak detection and constant fraction discrimination. The two first principles are more common in real laser radar systems while the matched filer is common in telecommunication applications [14]. One reason why matched filter is uncommon in laser radar applications is that for many applications the performance of peak detection and constant fraction have been good enough, especially in single-pixel systems. The new generation scanning and staring laser radar systems give other opportunities in object recognition and reconstruction where the object details can be extracted and used. Another aspect is the sampling frequency, in telecommunication the sampling frequency can be up to a few tens of MHz while in laser radar systems the frequencies lies in the GHz domain. To perform matched filtering in real time at those speeds is today not practically possible. There may be applications where the data accuracy is so important that the cost of memory, hardware implementations, and post-processing is worth the effort. The accuracy in peak detection and constant fraction can also be improved if the bias and variance that these detection principles produce is taken into account.

9 Conclusions

In this paper, laser radar cross section models for plane, cone, sphere, and parabola have been derived. The cross section models are used, in simulations, to analyze the impact of uncertainties in time-of-flight estimations. Three time-of-flight estimation algorithms have been analyzed; peak detection, constant fraction detection, and matched filter.

These simulations show that the estimation error can be assumed to have Gaussian distribution. This is an important result in laser radar system and laser radar data modeling.

For all shapes, the peak detection has a very large standard deviation compared to constant fraction detection and matched filter detection. The results for the plane indicates that constant fraction detection is not satisfactory when

the received pulse is broadened. The range estimation error is very small for both spheres and parabolas. Also in these cases the matched filter has the best performance. Naturally, the mean and standard deviation of the estimation error decreases when the SNR increases. The matched filter is less affected by the noise compared to the other detection methods. The peak detection method has a rather large standard deviation even when the SNR is high.

Also in the case on shape fitting the matched filter is less affected by the noise compared to the other detection methods. For line fitting the Cramér-Rao lower bound is calculated and the matched filter simulation results are close to this bound.

Acknowledgement

The authors acknowledge Åsa Persson, FOI, for information about the TopEye System.

References

[1] L.C. Andrews, R.L. Phillips, and C.Y. Young. *Laser Beam Scintillation with Applications*. SPIE Optical Engineering Press, Bellingham, 2001.

[2] W. Gander, G.H. Golub, and R. Strebel. Least-squares fitting of circles and ellipses. *BIT*, 34:558–578, 1994.

[3] W. Gander and U. Von Matt. *Solving Problems in Scientific Computing Using Maple and Matlab*, chapter 6: Some Least Squares Problems, pages 83–101. Springer, Berlin, 3rd edition, 1997.

[4] D.R. Gerwe and P.S. Idell. Cramér-Rao analysis of orientation estimation: Viewing geometry influences on the information conveyed by target features. *Journal of Optical Society of America A*, 20(5):797–816, May 2003.

[5] J.W. Goodman. A random walk through the field of speckle. *Optical Engineering*, 25(5):610–612, May 1986.

[6] C. Grönwall, T. Carlsson, and F. Gustafsson. Performance analysis of measurement error regression in direct-detection laser radar imaging. In *Proceedings IEEE Conference on Acoustics, Speech and Signal Processing*, volume VI, pages 545–548, Hong Kong, April 2003.

[7] C. Grönwall and F. Gustafsson. Modelling of laser radar systems. Technical Report LiTH-ISY-R-2743, Dept. of Electrical Engineering, Linköpings Universitet, Linköping, Sweden, Sep. 2006.

[8] S. Van Huffel and J. Vandewalle. *The Total Least Squares Problem. Computational Aspects and Analysis*. SIAM, Philadelphia, 1991.

[9] A. Jain, P. Moulin, M.I. Miller, and K. Ramchandran. Information-theoretic bounds on target recognition performance based on degraded image data. *IEEE Transactions on Pattern Analysis and Machine Intelligence*, 24(9):1153– 1166, 2002.

[10] A.V. Jelalian. *Laser Radar Systems.* Artech House, Norwood, MA, 1992.

[11] S.M. Kay. *Fundamentals of Statistical Signal Processing: Estimation Theory*, volume 1. Prentice Hall, Upper Saddle River, NJ, 1993.

[12] J. Khoury, C.L. Woods, J. Lorenzo, J. Kierstead, D. Pyburn, and S.K. Sengupts. Resolution limits in imaging laser radar systems. *Applied Optics*, 45(4):697–704, 2006.

[13] A.E. Koksal, J.H. Shapiro, and M.I. Miller. Performance analysis for ground-based target orientation estimation: FLIR/LADAR sensor fusion. In *Conference Record of the Thirty-Third Asilomar Conference on Signals, Systems, and Computers*, volume 2, pages 1240 –1244, October 1999.

[14] J.G. Proakis. *Digital Communications, 3rd Ed.* McGraw-Hill, 1995.

[15] I. Prochazka, K. Hamal, and L. Kral. Atmospheric fluctuation induced laser ranging jitter. In *Proceedings SPIE*, volume 5575, pages 155–160, 2004.

[16] D.L. Snyder and A.M. Hammoud. Image recovery from data acquired with a charge-coupled-device camera. *Journal of the Optical Society of America, A*, 10(5):1014–1022, 1993.

[17] O. Steinvall. Effects of target shape and reflection on laser radar cross sections. *Applied Optics*, 39(24):4381–4391, August 2000.

[18] O. Steinvall and T. Chevalier. Range accuracy and resolution for laser radars. In *Proceedings SPIE*, volume 5988, pages 73–88, October 2005.

[19] O. Steinvall, T. Chevalier, and H. Larsson. Data collection and simulation of high range resolution laser radar for surface mine detection. In *Proceedings SPIE*, volume 6214, pages 85–102, May 2006.

Avdelning, Institution
Division, Department

Division of Automatic Control
Department of Electrical Engineering

Datum
Date

2006-10-16

Språk
Language

☐ Svenska/Swedish
☒ Engelska/English

☐ _____

Rapporttyp
Report category

☐ Licentiatavhandling
☐ Examensarbete
☐ C-uppsats
☐ D-uppsats
☒ Övrig rapport
☐ _____

ISBN
—

ISRN
—

Serietitel och serienummer
Title of series, numbering

ISSN
1400-3902

LiTH-ISY-R-2745

URL för elektronisk version

http://www.control.isy.liu.se

Titel
Title

Influence of Laser Radar Sensor Parameters on Range Measurement and Shape Fitting Uncertainties

Författare
Author

Christina Grönwall, Ove Steinvall, Fredrik Gustafsson, Tomas Chevalier

Sammanfattning
Abstract

In object reconstruction and recognition based on laser radar data, the range value's accuracy is important. The range data accuracy depends on the accuracy in the laser radar's detector, especially the algorithm used for time-of-flight estimation. In this paper, we model a general direct-detection laser radar system applicable for hard target measurements. We derive the time and range dependent laser radar cross sections for some simple geometric shapes (plane, cone, sphere, and parabola). The cross section models are used, in simulations, to find the proper statistical distribution of uncertainties in time-of-flight range estimations. Three time-of-flight estimation algorithms are analyzed; peak detection, constant fraction detection and matched filter. The detection performance for various shape conditions and signal-to-noise ratios are analyzed. Two simple shape reconstruction examples are shown, and the detector's performances are compared with the Cramér-Rao lower bound. The performance of the peak detection and the constant fraction detection is more dependent on the shape and noise level, compared to the matched filter. For line fitting the matched filter perform close to the Cramér-Rao lower bound.

Nyckelord
Keywords

Range error, laser radar, time-of-flight, peak detection, matched filter, performance.